PROBING THE OPTICAL PROPERTIES AND ELECTRONIC STRUCTURE OF PEPTIDE COATED GOLD NANOPARTICLES ON LANTHANUM ALUMINATE USING SPECTROSCOPY ELLIPSOMETRY

SOH WEI JIE JEREMY

NATIONAL UNIVERSITY OF SINGAPORE

2016

PROBING THE OPTICAL PROPERTIES AND ELECTRONIC STRUCTURE OF PEPTIDE COATED GOLD NANOPARTICLES ON LANTHANUM ALUMINATE USING SPECTROSCOPY ELLIPSOMETRY

Soh Wei Jie Jeremy

(*B.Sc. (Hons.), NUS*)

A THESIS SUBMITTED

FOR THE DEGREE OF BACHELOR OF SCIENCE

(HONS.) IN PHYSICS

DEPARTMENT OF PHYSICS

NATIONAL UNIVERSITY OF SINGAPORE

2016

DECLARATION

I hereby declare that the thesis is my original work and it has been written by me in its entirety. I have duly acknowledged all the sources of information which have been used in the thesis.

This thesis has also not been submitted for any degree in any university previously.

Soh Wei Jie Jeremy
4th April 2016

Acknowledgment

I would like to express my gratitude to Dr. Andrivo Rusydi for his encouragement and guidance on this project. In addition, I would like to thank Dr. David Paramelle, Dr. Teguh Citra Asmara and Jason Lim Chee Wai for their professional support throughout this project. Last but not least, I would like to thank Tan Tu Guang and Lai Junhao for the invaluable discussion.

Contents

Abstract

The dielectric function of $LaAlO_3$ was extracted from the ellipsometry parameters ψ and Δ using the pseudo dielectric function. Error propagation was applied to $\delta\psi$ and $\delta\Delta$, where $\delta\epsilon$ is obtained. This was necessary for RefFIT to compute for chi-square χ^2. Fitting procedures were conducted in RefFIT as illustrated in Section 3.1.3. The Lorentz oscillators obtained from the $LaAlO_3$ fit were used as part of the fitting procedure for the gold nanoparticles on $LaAlO_3$ substrate. The large χ^2 and a significant percentage difference of ϵ_2 from 0.6 to 0.9 eV suggests the presence of anisotropy in $LaAlO_3$. We compare the experimental ϵ_1 and ϵ_2 to the experimental values and FP-LAPW by X. Luo et al. Using our experimental data as well as the experimental band gap of $LaAlO_3$, the experiment ϵ_2 from X. Luo et al. below 5.6 eV is inaccurate to a large extent.

List of Figures

Chapter 1

Introduction

Gold nanoparticle can be used as a biosensor due to its rich localized surface plasmon resonance properties and its functionalization properties. However, gold nanoparticles tend to aggregate when they are exposed to electrolytes in the biological environment. In addition, functional groups that bind strongly to gold are present. These will affect their colloidal stability, where the gold nanoparticles lose their function as a biosensor.

Ligand shells are introduced as a capping agent to protect the gold nanoparticles in the biological environment. A pentapeptide ligand, CALNN illustrated in Fig. 1.1 is used as the capping agent for the gold nanoparticles based on protein folding considerations. The principle for the design is as follows: The head of the ligand that is exposed to the environment is a hydrophilic group, while the tail of the ligand must be able to bond with the gold nanoparticle. The design criteria establishes the need for the capping agent to attach to the gold nanoparticle via a thiol group.

The side chain of Cysteine (C) has a thiol group that can form a covalent bond with gold. Alanine (A) and Leucine (L) are chosen for position 2 and 3 due to their hydrophobic side chains for self-assembly. Taking into account the curvature of the nanoparticle, the side chain of Leucine is larger than that of Alanine. Asparagine (N) is chosen for position 4 and 5 as it is uncharged and hydrophilic. The negative charge at the C-terminus provides repulsion to prevent aggregation of the nanoparticles.

CALNN stabilizes the gold nanoparticles against electrolyte-induced aggregation, but increases the possibility of non specific binding with proteins that are positively charged. In addition, ligand exchange with thiolated pentapeptides occurs with this capping agent. The Mix-matrix ligand shell is introduced to solve these issues. It is composed of 70 % peptidol H-CVVVT-ol (V: Valine, T: Threonine) and 30 % ethylene glycol-terminated alkane-thiol HS-$C_{11} - EG_4$. With the Mix-matrix ligand shell, the resistance to non-specific binding and ligand exchange improves drastically. [6] [1]

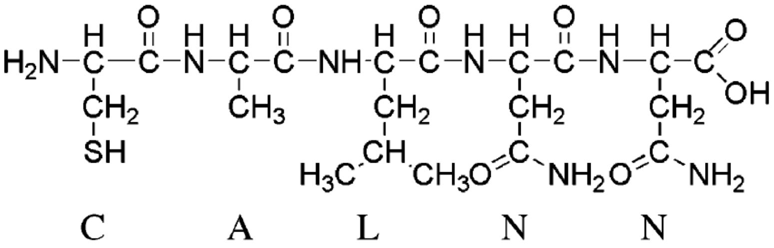

Fig. 1.1. Structure of CALNN. Extracted from [1]

As mentioned earlier, the ligand shell are capped over the gold nanoparticles via the thiols. To be more precise, this interaction is mediated through the sulfhydryl (SH) functional group. It is crucial to understand the chemistry and structure of this interface, as they control the system properties such as ligand-exchange reactions. Many efforts have been made to study the sulphur-gold interface. However, the atomic level of this interface remains elusive and controversial. [7] [8]

For this project, we would like to understand the sulphur gold interface using spectroscopic ellipsometry. The peptide coated gold nanoparticles solution is placed on the Lanthanum Aluminate ($LaAlO_3$) substrate, where the complex dielectric functions is obtained. For this part of the project, we would need to analyse the $LaAlO_3$ substrate. Next, we analyse the citrate coated gold nanoparticles solution placed on the $LaAlO_3$ substrate. Using a simplified optical model, we extract the relevant optical properties of the $LaAlO_3$ substrate and citrate coated gold nanoparticles. This part of the project would serve as a preliminary analysis, where we hope to obtain the relevant directions for future work.

1.1 Principle of Optics

The propagation of light in a media could be described by the complex refractive index as follows:

$$N \equiv n - ik \tag{1.1}$$

where n is the refractive index and k is the extinction coefficient. [3]

1.2 Dielectric

1.2.1 Dielectric Polarization

When an external electric field is applied in a dielectric, the spatial distributions of the electric charges undergo a slight modification. This phenomenon represents a dielectric polarization, which is used to determine the complex refractive index. There exists several types of dielectric polarization such as the electric polarization and the ionic polarization.

Fig. 1.2 illustrates the electric polarization. In the absence of an external electric field, the atom has no net dipole moment as the centre of mass of the negatively charged electron cloud coincides with that of the positively charged nucleus. When an external electric field is applied, the electron cloud is displaced slightly away from the nucleus. This results in an induced dipole moment.

Fig. 1.3 illustrates the ionic polarization of a NaCl chain in the NaCl crystal. In the absence of an external electric field, the dipole moment p_+ and

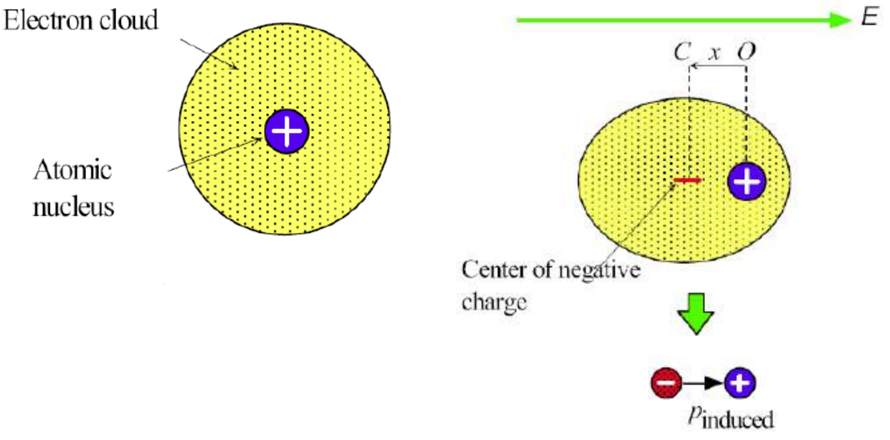

(a) (b)

Fig. 1.2. (a) Atom has no net dipole moment. (b) Net dipole moment induced in the presence of an external electric field. Extracted from [2]

the dipole moment p_- have equal magnitude. This results in a zero net dipole moment per ion. When an external electric field is applied in the positive x direction, the Na^+ ions are shifted in the positive x direction, while the Cl^- ions are shifted in the negative x direction. This led to an increase in the dipole moment p_+ and a decrease in the dipole moment p_-, resulting in a net dipole moment per ion.

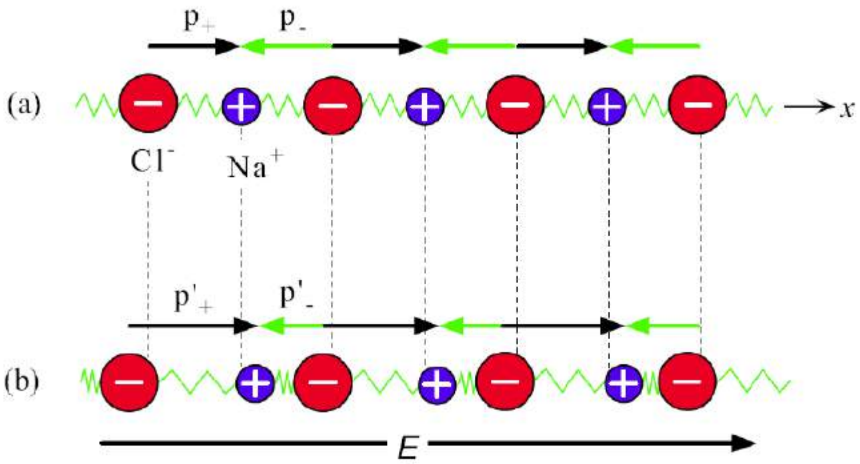

Fig. 1.3. NaCl chain in the NaCl crystal. (a) No net dipole moment per ion. (b) Net average induced dipole moment per ion in the presence of an external electric field. Extracted from [2]

Fig. 1.4 illustrates the electric dipole radiation in a dielectric. When light wave propagates in the dielectric, electric dipole radiation occurs. The sinusoidal ac electric field component acts as a time-varying electric field, causing the electric dipoles to accelerate. This leads to the emission of electromagnetic radiation with the same frequency as the incident light wave by the electric dipole.

The electric dipole at different stages when the time varying electric field acts on the dielectric is illustrated in Fig. 1.4. In stage 1, the positive charge is displaced upwards, while the negative charge is displaced downwards. The displacement occurs at a greater extent in stage 2. The amplitude of the electric field decreases in stage 3, leading to a smaller extent in the displacement. In stage 4, there is no external electric field acting on the dielectric, thus the centre of mass for the opposite charges coincide. In stage 5, the displacement occur in a different direction as the direction of the electric field changes. The acceleration of the electric dipole leads to electromagnetic radiation in (g). [3][2]

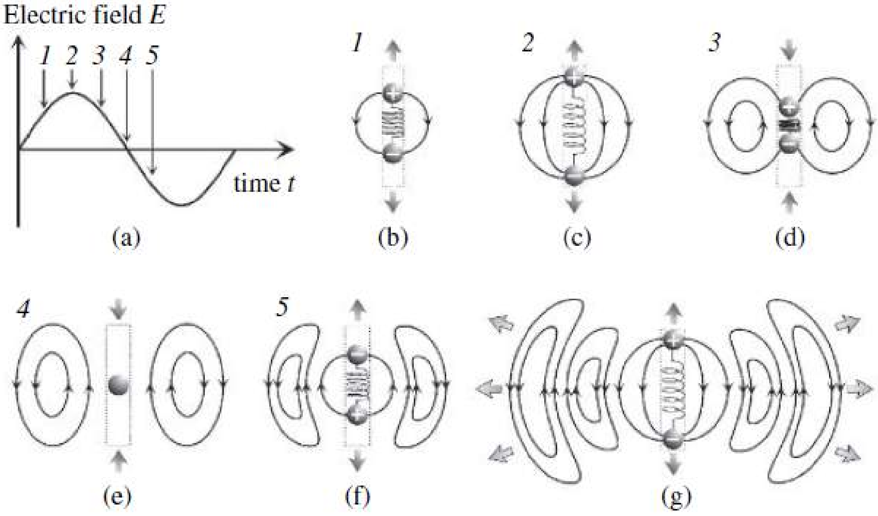

Fig. 1.4. Electric Dipole Radiation in a dielectric. Extracted from [3]

1.2.2 Complex Dielectric Function

The complex refractive index is defined as:

$$N^2 \equiv \epsilon \tag{1.2}$$

where the complex dielectric function ϵ is defined by

$$\epsilon \equiv \epsilon_1 + i\epsilon_2 \tag{1.3}$$

From equation 1.1, 1.2 and 1.3, we obtain the real and imaginary part of ϵ

$$\epsilon_1 = n^2 - k^2 \tag{1.4}$$

$$\epsilon_2 = 2nk \tag{1.5}$$

Fig. 1.5 illustrates the real component ϵ_1 and imaginary component ϵ_2 of the dielectric function plotted against the angular frequency of light logω. The dielectric function in this figure is represented by the Lorentz model. At low ω, ϵ_1 is represented by the static dielectric constant ϵ_s. When ω is higher than the infrared region, ϵ_1 is represented by the high frequency dielectric constant ϵ_∞. At an even higher ω, the value of ϵ_1 is 1 (vacuum). The atomic (ionic) polarization contributes to ϵ_s - ϵ_∞, while the electric polarization contributes to ϵ_∞ - 1.

The dielectric polarization is modeled by the oscillation of springs. Resonance oscillation occurs when the angular frequency of light and spring coincides. This results in the absorption at light by the medium. This is represented by the peak of ϵ_2. The resonant oscillation for atomic and electric polarization is generally observed in the infrared and vis/uv region respectively. ϵ_1 is considered the polarization term, while ϵ_2 is related to absorption.

For metals, light absorption occurs due to the free carriers. The dielectric function is represented by the dashed lines in Fig. 1.5. ϵ_1 have negative values below the plasma angular frequency ω_p. At lower ω, the increase in ϵ_2 is caused by the free carrier absorption. [3]

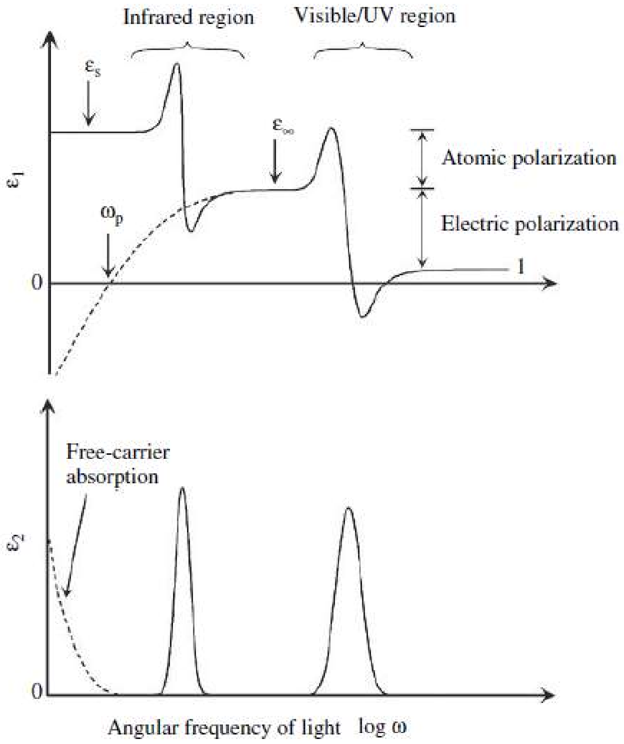

Fig. 1.5. The real and imaginary part of ϵ plotted against the angular frequency of light log ω with reference to the Lorentz model.Extracted from [3]

1.3 Fresnel Equations

Polarization of light consists of p- and s-polarized light waves. Fig. 1.6 illustrates the reflection of p- and s-polarized light waves at an interface. The electric field of p-polarized light oscillates within the plane of incidence, while the oscillation of the electric field of s-polarized light is perpendicular to the plane of incidence.

Fig. 1.7 illustrates the reflection and transmission of p- and s-polarized light waves. This is represented with the electric field **E** and magnetic induction

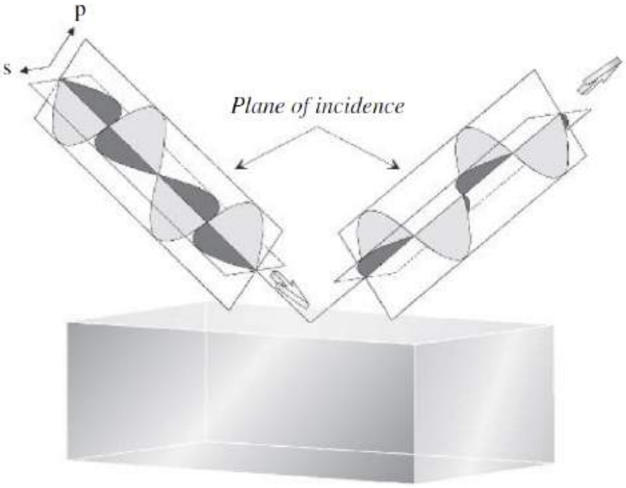

Fig. 1.6. Reflection of p- and s-polarized light waves at an interface. Extracted from [3]

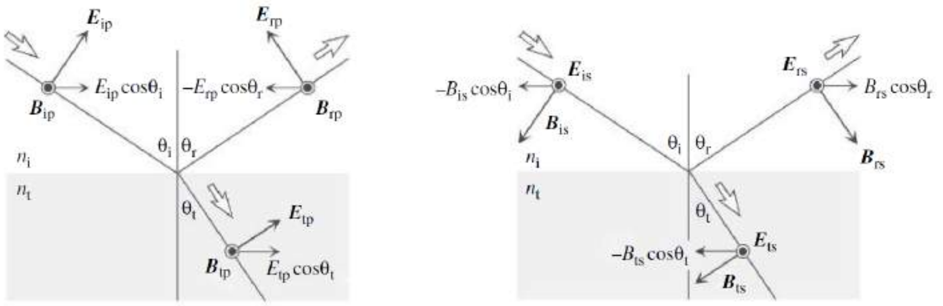

(a) (b)

Fig. 1.7. Representation of Electric field **E** and Magnetic Induction **B** for Reflection and Transmission of (a) p- and (b) s-polarized light waves. Extracted from [3]

B. The subscript i, r and t denotes the incidence, reflection and transmission side respectively. At the interface, the boundary conditions require the **E** and **B** components that are parallel to the interface to be continuous. With the boundary conditions, the equations for the amplitude reflection coefficients r_p and r_s as well as the amplitude transmission coefficient t_p and t_s could be obtained. These are known as the Fresnel equations.

N could replace n in the equation, which results in a complex amplitude coefficient. The amplitude reflection coefficients r_p and r_s are expressed as

$$r_p = \frac{N_{ti}^2 \cos\theta_i - (N_{ti}^2 - sin^2\theta_i)^{\frac{1}{2}}}{N_{ti}^2 \cos\theta_i + (N_{ti}^2 - sin^2\theta_i)^{\frac{1}{2}}} \tag{1.6}$$

$$r_s = \frac{\cos\theta_i - (N_{ti}^2 - sin^2\theta_i)^{\frac{1}{2}}}{\cos\theta_i + (N_{ti}^2 - sin^2\theta_i)^{\frac{1}{2}}} \tag{1.7}$$

where θ_i is the angle of incidence, $N_{ti} = \frac{N_t}{N_i}$, N_t and N_i are complex refractive index for the transmission and incidence side respectively. [3]

1.4 Principles of Spectroscopy Ellipsometry

Fig. 1.8 illustrates the ellipsometry measurement, where the amplitude ratio and the phase difference between p- and s- polarizations (ψ, Δ) are measured. Fig. 1.9 illustrates ψ and Δ in the coordinate system.

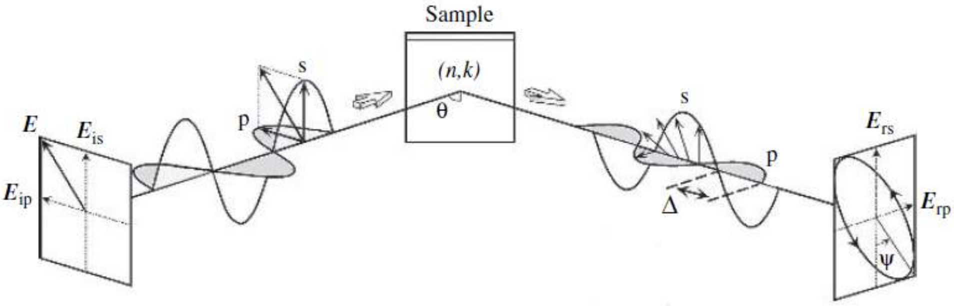

Fig. 1.8. Ellipsometry Measurement. Extracted from [3]

The measured (ψ, Δ) are defined as

$$\rho \equiv \tan\psi \exp(i\Delta) \equiv \frac{r_p}{r_s} \tag{1.8}$$

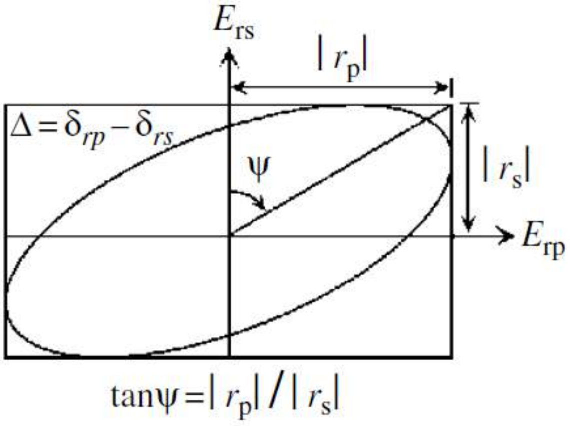

Fig. 1.9. Coordinate System in Ellipsometry. Extracted from [3]

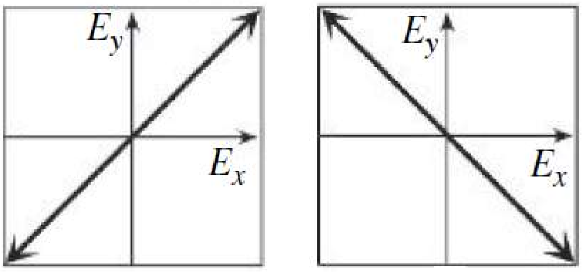

(a) (b)

Fig. 1.10. Polarization state for (a) $\Delta = 0°$ and (b) $\Delta = 180°$. Extracted from [3]

1.5 Pseudo Dielectric Function

The pseudo dielectric function $\langle\epsilon\rangle$ represents the dielectric function of a perfect substrate with infinite thickness. It can be calcuated from the ellipsometry parameters in (1.8):

$$\langle\epsilon\rangle = sin^2\theta_i \left[1 + tan^2\theta_i \left(\frac{1-\rho}{1+\rho}\right)^2\right] \tag{1.9}$$

$$\langle\epsilon\rangle = \langle\epsilon_1\rangle - i\langle\epsilon_2\rangle \tag{1.10}$$

1.6 Dielectric Function Model

1.6.1 Lorentz Model

Lorentz model represents the motion of the electron with respect to the nucleus as a spring. It is represented by

$$\epsilon(\omega) = 1 + \frac{\omega_p^2}{\omega_o^2 - \omega^2 + i\gamma_o\omega} \tag{1.11}$$

where ω_p, ω_o and γ_o denotes the plasma frequency, resonance frequency and the line width of the oscillator respectively.

We approach the limit 0,∞ and obtain

$$\epsilon_s = \epsilon(\omega \longrightarrow 0) = 1 + \frac{\omega_p^2}{\omega_o^2} \tag{1.12}$$

$$\epsilon_\infty = \epsilon(\omega \longrightarrow \infty) = 1 \tag{1.13}$$

Combining (1.11), (1.12) and (1.13), we obtain

$$\epsilon_s = \epsilon_\infty + \frac{\omega_p^2}{\omega_o^2} \tag{1.14}$$

$$\epsilon(\omega) = \epsilon_\infty + \frac{\omega_p^2}{\omega_o^2 - \omega^2 + i\gamma_o\omega} \tag{1.15}$$

1.6.2 Sellmeier Model

At $\omega << \omega_o$, γ_o approaches zero in the region where ϵ_2 is approximately zero. From 1.15, the Sellmeier model is expressed as

$$\epsilon(\omega) = \epsilon_\infty + \frac{\omega_p^2}{\omega_o^2 - \omega^2} \tag{1.16}$$

1.6.3 Data Analysis Procedure

An optical model is constructed for the sample. Next, the dielectric function for the different layers are selected or modeled. The modeel spectra is fitted experimental spectra, and the fitting error is calculated. Chi-Square χ^2 is calculated with the following equation:

$$\chi = \frac{1}{\sqrt{M-P-1}} \left\{ \sum_{j=1}^{M} \left[\frac{\rho_{ex}(hv_j) - \rho_{cal}(hv_j)}{\delta\rho(hv_j)} \right]^2 \right\}^{1/2} \tag{1.17}$$

where M and P are the number of measurements and analytical parameter respectively. This could be applied to ψ, Δ and $\langle\epsilon\rangle$ as well.

The procedure aims to minimize the fitting error. When this value is large, the optical model is revised. A different dielectric function could be applied as well. The optical parameters are determined when the fitting error is minimized. [3]

1.7 Lanthanum Aluminate

Lanthanum Aluminate ($LaAlO_3$) has a perovskite structure, and serves as a common substrate material.Fig. 1.11 illustrates the cubic structure of $LaAlO_3$ at 813 K. At room temperature, the structure of $LaAlO_3$ is rhombohedral. This phase transition is attributed to the rotation of Al-O_6 octahedra along the (111) cubic unit direction. The La atoms are 12 fold with respect to the O atoms. The lattice parameters of $LaAlO_3$ are a = b = 5.370 $\mathring{A}$ and c = 13.138 $\mathring{A}$.

We could view $LaAlO_3$ as an alternating sublayers AlO_2 and LaO as illustrated in Fig. 1.12. The valence of La and Al is 3+, while that of O is 2-. Therefore, the valence of AlO_2 and LaO sublayers are +1 and -1 respectively. By splitting the valence equally to the top and bottom surface of the sublayers, the regions between the sublayers have zero valence. As

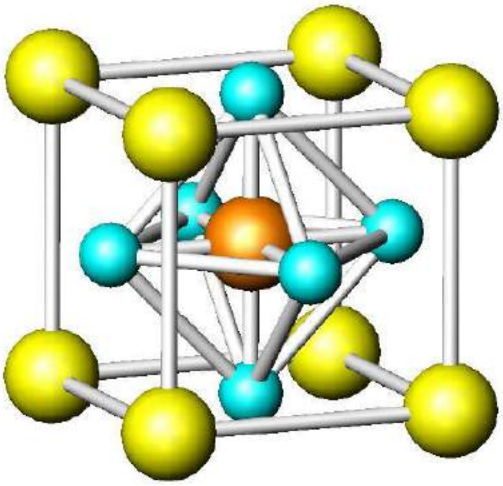

Fig. 1.11. Cubic $LaAlO_3$ at 813 K. The atom in yellow, orange and blue represents La, Al and O respectively. Extracted from [4]

a result, the valence is unbalanced at the surface, which gives rise to the polar nature of $LaAlO_3$.

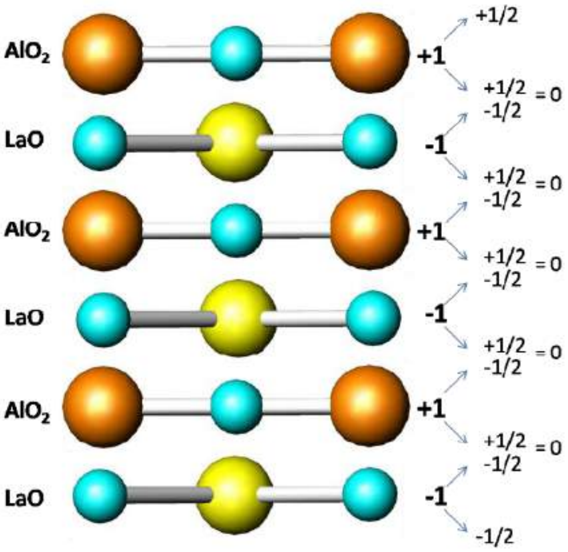

Fig. 1.12. Alternating sublayers AlO_2 and LaO within a bulk $LaAlO_3$ in the $< 001 >$ directions. Atoms in yellow, orange and blue are La, Al and O respectively. Extracted from [4]

$LaAlO_3$ has two types of polarization. The electric polarization is contributed by the La, Al and O atoms, while the ionic polarization is contributed by the $(LaO)^+$ and $(AlO_2)^-$ sublayers. In Fig. 1.13, electronic density distribution of rhombohedral $LaAlO_3$ was illustrated. We observe a mixture of charge density between La-O and Al-O atoms. There exists a strong directional bonding for Al-O, while the bonding for La-O is weaker due to the relative sparse hybridizations. This directionality suggests an anisotropic property. In addition, the bonding behavior of $LaAlO_3$ consists of ionic and covalent nature. This is based on the Mulliken charges and bond population of $LaAlO_3$. [4] [5][9]

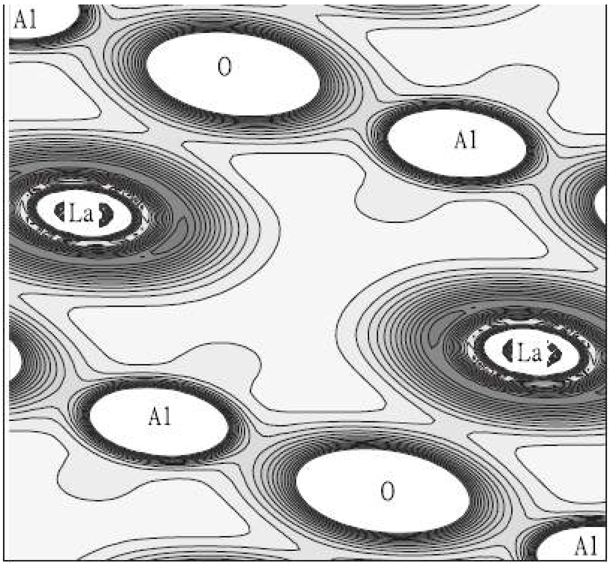

Fig. 1.13. Electronic Density distribution of rhombohedral $LaAlO_3$ in a (110) plane. Extracted from [5]

Chapter 2

Methodology

2.1 Data Analysis of Lanthanum Aluminate substrate

The ellipsometry parameters ψ and Δ for the $LaAlO_3$ substrate were provided by Dr. Teguh Citra Asmara. The measurements were taken with Wollam V-VASE Spectroscopic Ellipsometry using reflection mode at room temperature with a polarizer angle of 45°. The angle of incidence were 50°, 60°, 70° and 80° from the sample normal. The data was taken within an energy range of 0.60 - 6.50 eV. For 60° and 70°, the data points from 6.35 to 6.5 eV data were not present in the data as the reflected intensity was too low for detection. The light beam spot size was about 1 to 3 mm in diameter. The sample was aligned until the light beam was focused on the surface of the sample. Any side tilting was minimized.

The bulk crystalline $LaAlO_3$ sample was obtained from CrysTec GmbH with 99.99% purity. The sample was one-sided polished to minimized back reflection. The orientation, surface dimension and thickness was (001), 10 mm by 10 mm and 0.5 mm respectively.

The dielectric function ϵ was extracted from the ellipsometry parameters ψ and Δ using the pseudo dielectric function approach. $\delta\epsilon_1$ and $\delta\epsilon_2$ were obtained by applying error propagation to $\delta\psi$ and $\delta\Delta$. RefFIT was used to fit the experimental dielectric function to the Lorentz model. Analysis were conducted with the experimental and fitting parameters.

2.2 RefFIT

RefFIT is a software designed by Dr. Alexey Kuzmenko to fit optical spectra. It is based on the Levenberg-Marquardt algorithm of chi-square χ^2 minimization, where it balances between the 'gradient descent' and 'inverse Hessian'. The experimental spectra is fitted to a dielectric function model with adjustable parameters, where the variation of parameters are driven by chi-square χ^2 minimization to obtain the best fit between the experimental and model data points.

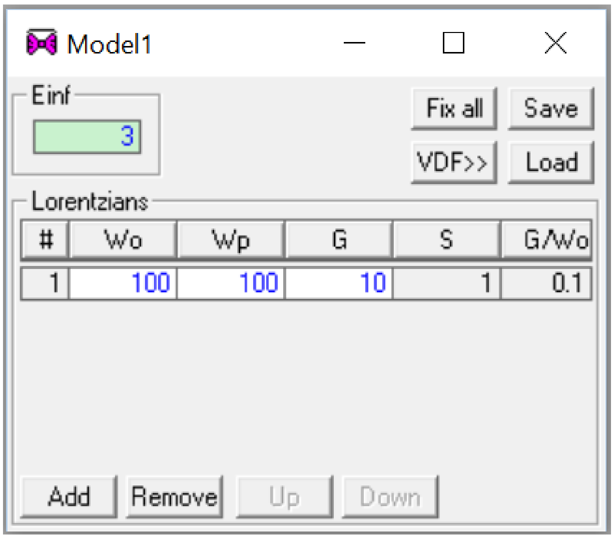

Einf: 3

Lorentzians

#	Wo	Wp	G	S	G/Wo
1	100	100	10	1	0.1

Fig. 2.1. RefFIT model parameters.

RefFIT uses (1.15) as its fundamental dielectric function model. Fig. 2.1 illustrates the RefFIT model parameters. E_{inf} represents high frequency dielectric constant ϵ_{∞}. The Lorentz oscillator parameters W_o, W_p and G are ω_o ω_p and γ_o in (1.15) respectively. They are measured in inverse centimeters (cm^{-1}). Lastly, S represents $\frac{\omega_p^2}{\omega_o^2}$ in (1.14) describing the atomic polarization.

The parameters above are representative of the Lorentz model. Special optical models and dielectric function models exist as well, where special inputs are used. One have to take note that the meaning of the parameters are different depending on the model.

2.3 Experiment Setup of Gold Nanoparticles

Fig. 2.2 illustrates the experimental setup. Using a pipette, two drops of the citrate coated gold nanoparticles solution were placed on the $LaAlO_3$ substrate. A tweezer was used to transfer the sample onto the mount. Measurements of ψ and Δ were taken with Sentech SE 80. The angle of incidence were 50°, 60° and 70° from the sample normal, and the data was taken within an energy range of 0.49 - 6.50 eV. The sample was aligned until the light beam was focused on the surface of the sample. Any side tilting was minimized. 2 sets of measurements were collected from this setup.

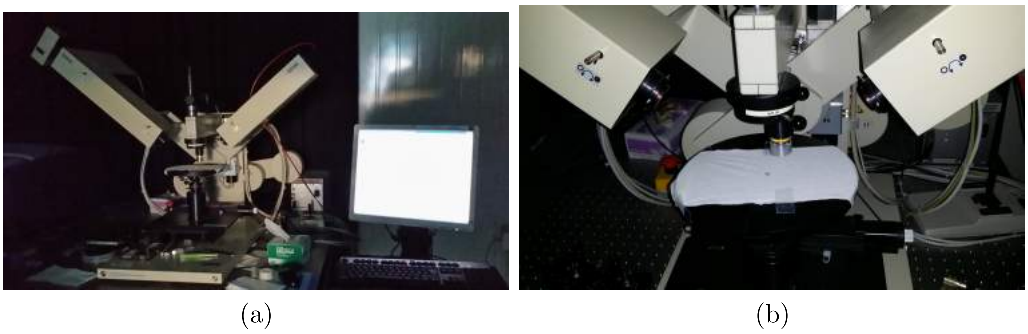
(a)

(b)

Fig. 2.2. Experiment Setup of Gold Nanoparticle solution on $LaAlO_3$ substrate. (a) Sentech SE 80 setup. (b) Sample on the mount.

2.4 Preliminary Analysis of Gold Nanoparticles

During the first set of measurements, we observed a reduction of volume in the gold nanoparticle solution. A second set of measurements was conducted, where we observed a 'stain' of gold nanoparticles solution instead of the initial two drops of gold nanoparticle solution. The second set would be a more consistent setup during the measurements for the different angle, as compared to the first set. The ellipsometry parameters were compared between the two data sets. Using the second set of measurements, we attempt to fit ψ and Δ of gold nanoparticle solution on $LaAlO_3$ substrate in RefFIT.

Chapter 3

Results and Discussion

3.1 Lanthanum Aluminate substrate

Fig. 3.1 illustrates the ψ and Δ of $LaAlO_3$ substrate from 0.6 to 6.35 eV. For ψ, we observe an increasing trend with photon energy for 50° and 60°, and a decreasing trend for 70° and 80°. For Δ, we observe a decreasing trend with photon energy for 50° and 60°, and an increasing trend for 70° and 80°. The polarization state at $\Delta = 0°$ and 180° is linear as illustrated in Fig. 1.10. The linear polarization deviates towards an elliptical polarization as photon energy increases. For 70°, Δ deviates towards an elliptical polarization to a greater extent from 4 eV.

3.1.1 Pseudo Dielectric Function

By applying (1.8) and (1.9), $\langle\epsilon\rangle$ for $LaAlO_3$ substrate can be determined. Fig. 3.2 illustrates ϵ_1 and ϵ_2 of $LaAlO_3$ substrate from 0.6 to 6.35 eV. We observe an increasing trend for ϵ_1 and ϵ_2.

3.1.2 Error Propagation

The $\delta\langle\epsilon_1\rangle$ and $\delta\langle\epsilon_2\rangle$ were calculated from the error propagation of $\delta\psi$ and $\delta\Delta$ using equation (3.1) to (3.6). This will be used for the χ^2 calculation

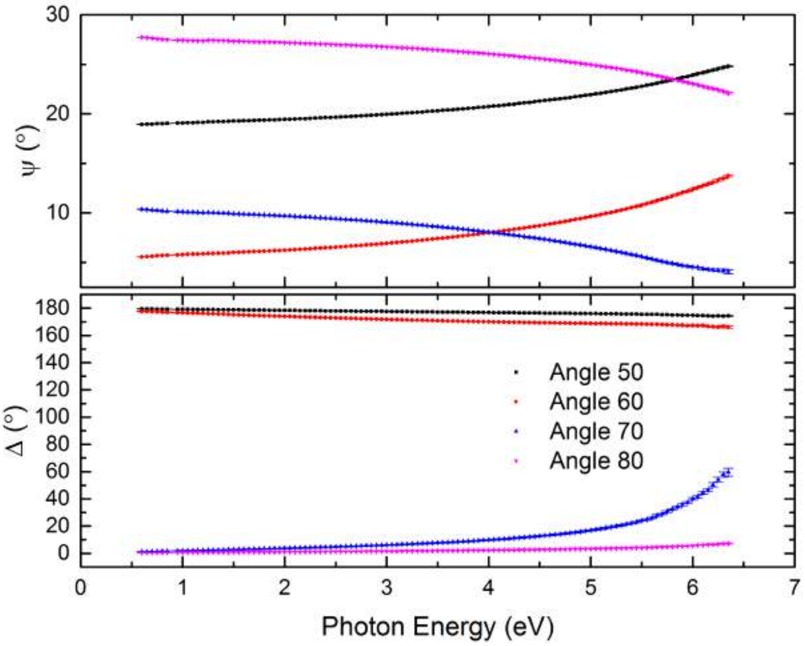

Fig. 3.1. ψ and Δ of $LaAlO_3$ substrate for 50°, 60°, 70° and 80° from 0.6 to 6.35 eV.

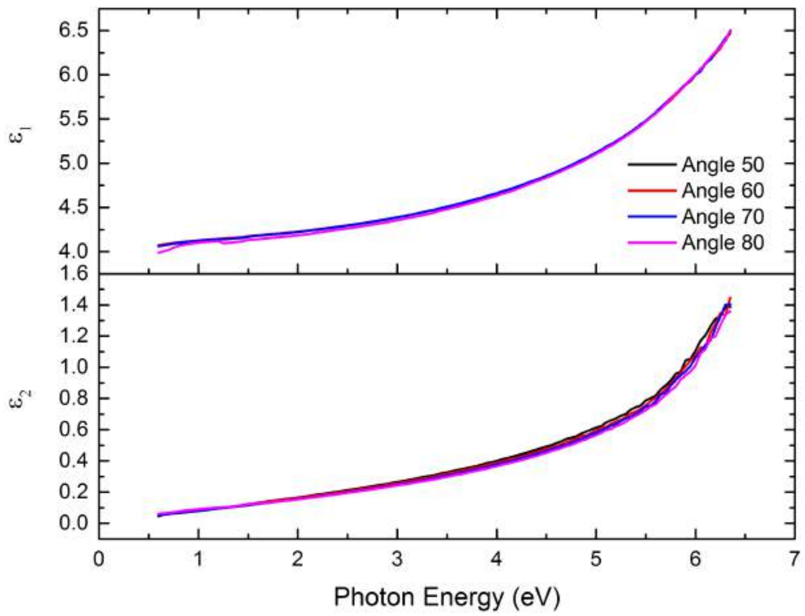

Fig. 3.2. ϵ_1 and ϵ_2 of $LaAlO_3$ substrate for 50°, 60°, 70° and 80° from 0.6 to 6.35 eV.

in RefFIT.

$$\delta\langle\epsilon\rangle = \sqrt{\left(\frac{\partial\langle\epsilon\rangle}{\partial\theta_i}\delta\theta_i\right)^2 + \left(\frac{\partial\langle\epsilon\rangle}{\partial\rho}\delta\rho\right)^2} \tag{3.1}$$

$$\begin{aligned}\frac{\partial\langle\epsilon\rangle}{\partial\theta_i} &= 2\sin\theta_i\cos\theta_i\left[1+\tan^2\theta_i\left(\frac{1-\rho}{1+\rho}\right)^2\right] \\ &\quad +2\sin^2\theta_i\tan\theta_i\sec^2\theta_i\left(\frac{1-\rho}{1+\rho}\right)^2\end{aligned} \tag{3.2}$$

$$\frac{\partial\langle\epsilon\rangle}{\partial\rho} = -4\sin^2\theta_i\tan^2\theta_i\left[\frac{1-\rho}{(1+\rho)^3}\right] \tag{3.3}$$

$$\delta\rho = \sqrt{\left(\frac{\partial\rho}{\partial\psi}\delta\psi\right)^2 + \left(\frac{\partial\rho}{\partial\Delta}\delta\Delta\right)^2} \tag{3.4}$$

$$\frac{\partial\rho}{\partial\psi} = \sec^2\psi\exp i\Delta \tag{3.5}$$

$$\frac{\partial\rho}{\partial\Delta} = i\tan\psi\exp i\Delta \tag{3.6}$$

3.1.3 Fitting for Angle 60

Using RefFIT, we fit the experimental dielectric function ϵ to the Lorentz model. Fig. 3.3 to Fig. 3.7 illustrates the approach used for fitting. The graph illustrates the plot of Epsilon (ϵ_1, ϵ_2) against wavenumber. The wavenumber is obtained using 1 eV = 8065.6 cm^{-1}. The green line, blue line, black square and red square denote ϵ_1 model, ϵ_2 model, ϵ_1 experiment and ϵ_2 experiment respectively.

We begin by fitting a Lorentz oscillator in Step 1. The experimental data did not fit well to the model from 45000 cm^{-1}. χ^2 was 67168, where ϵ_1 contributes significantly to the value. An additional oscillator was added in Step 2, and there was a decrease in χ^2 to 38897. We observe an increased contribution to χ^2 by ϵ_2. To improve the fitting in Step 3, we added the parameters of IR-active optical phonons provided in Infrared Lattice Dynamics of Lanthanum Aluminate by Travis et al.[10] The 5 sets of parameters are illustrated in 3.5, where they are highlighted in red. In RefFIT, the red parameters are fixed. χ^2 decreases significantly to 1184.22. In Step 4, we allow the parameters of the optical phonons to vary, limited to a range of 0 to 1000. In addition, two more oscillators were added for fitting. χ^2 decreases slightly to 1079.56. The first five oscillators belong to the variation of parameters from the optical phonons. The ω_o for the next four oscillators are 46230, 7504, 7504 and 67835. These are 5.7, 0.9, 0.9 and 8.4 eV respectively. $\omega_o = 5.7$ and 8.4 eV are above the experimental band gap of $LaAlO_3$: 5.6 eV.[12] These could be associated with the optical transition of O_{La}-2p to La-4f, 5d. [11] $\omega_o = 0.9$ eV should not exist, as ϵ_2 below the band gap is very close to zero.

Another constraint used to evaluate the fitting is 1.14. Using Einf and S in RefFIT, we are able to obtain ϵ_s. The value will be compared with the accepted values ranging from 19 to 25.[10] For step 4, $\epsilon_s = 5.88$ deviates from the accepted range. For step 5, two additional oscillators were added. χ^2 decreases to 694.354. The value of ϵ_s is 6.33, and the ω_o for the additional peaks are 0.6 and 1.2 eV. Fitting ends at Step 5, as the χ^2 starts to increase when extra oscillators were added.

χ^2 for Step 4 and 5 might be lower than that of Step 3, but the existence of ω_o below the band gap as well as the deviation of ϵ_s from the accepted range makes the fit infeasible. For step 3, ω_o of 8.3 and 9.0 eV are above the band gap, and the value of ϵ_s is 23.8. This will be a more appropriate fit compared to the other steps.

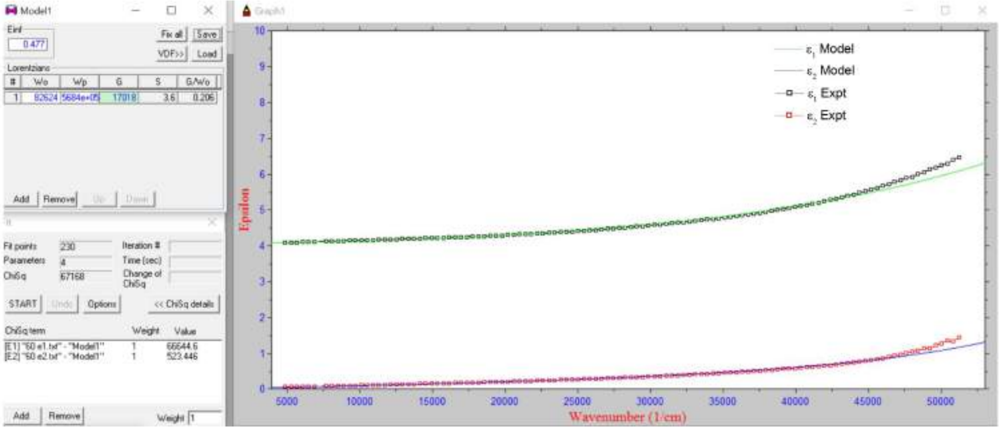

Model1

Einf 0.477

Lorentzians

#	Wo	Wp	G	S	G/Wo
1	82624	5684e+05	17018	3.6	0.206

Fit points 230

Parameters 4

ChiSq 67168

ChiSq term	Weight	Value
[E1] "60 e1.txt" - "Model1"	1	66644.6
[E2] "60 e2.txt" - "Model1"	1	523.446

Weight 1

Fig. 3.3. Fitting for Angle 60: Step 1.

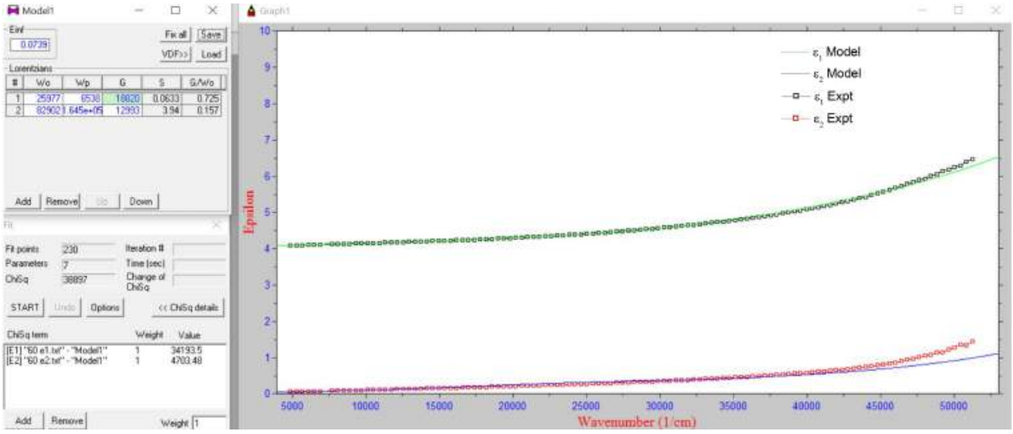

Model1

Einf 0.0739

Lorentzians

#	Wo	Wp	G	S	G/Wo
1	25977	6538	18820	0.0633	0.725
2	82902	1.645e+05	12993	3.94	0.157

Fit points 230

Parameters 7

ChiSq 38897

ChiSq term	Weight	Value
[E1] "60 e1.txt" - "Model1"	1	34193.5
[E2] "60 e2.txt" - "Model1"	1	4703.48

Weight 1

Fig. 3.4. Fitting for Angle 60: Step 2.

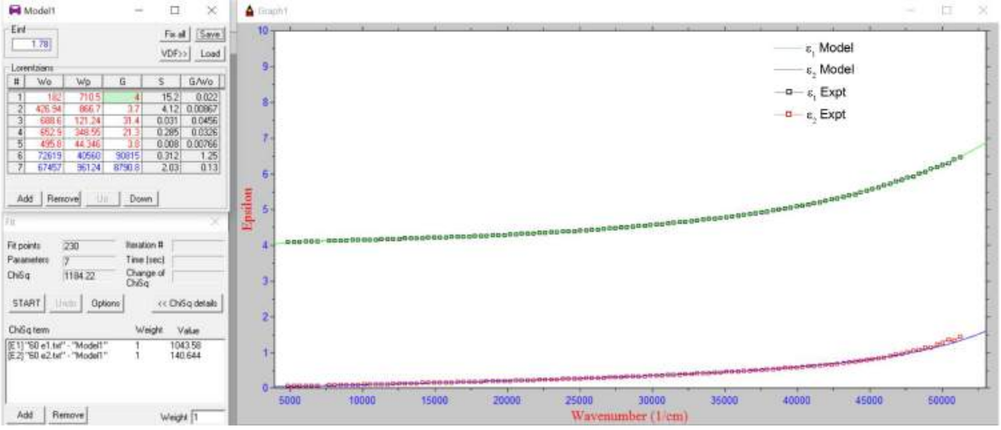

Model1

Einf 1.78

Lorentzians

#	Wo	Wp	G	S	G/Wo
1	182	710.5	4	15.2	0.022
2	426.94	866.7	3.7	4.12	0.00867
3	688.6	121.24	31.4	0.031	0.0456
4	652.9	348.55	21.3	0.285	0.0326
5	495.8	44.346	3.8	0.008	0.00766
6	72619	40560	90815	0.312	1.25
7	67457	96124	8790.8	2.03	0.13

Fit points 230

Parameters 7

ChiSq 1184.22

ChiSq term	Weight	Value
[E1] "60 e1.txt" - "Model1"	1	1043.58
[E2] "60 e2.txt" - "Model1"	1	140.644

Weight 1

Fig. 3.5. Fitting for Angle 60: Step 3.

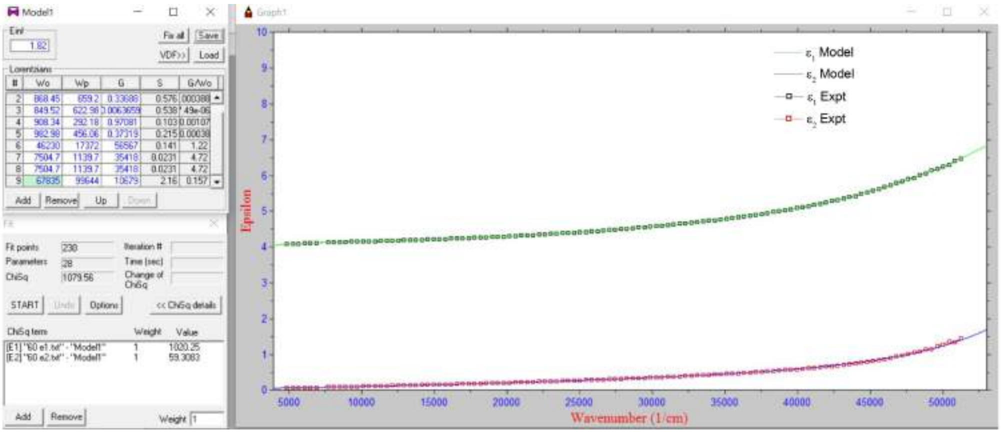

Einf 1.82

Lorentzians

#	Wo	Wp	G	S	G/Wo
2	868.45	659.2	0.33686	0.576	.000388
3	849.52	622.98	.0063659	0.538	49e-06
4	908.34	292.18	0.97081	0.103	0.00107
5	982.98	456.06	0.37319	0.215	0.00038
6	46230	17372	56567	0.141	1.22
7	7504.7	1139.7	35418	0.0231	4.72
8	7504.7	1139.7	35418	0.0231	4.72
9	67835	99644	10679	2.16	0.157

Fit points 230
Parameters 28
ChiSq 1079.56
Iteration #
Time (sec)
Change of ChiSq

ChiSq term	Weight	Value
[E1] "60 e1.txt" - "Model1"	1	1020.25
[E2] "60 e2.txt" - "Model1"	1	59.3083

Weight 1

Fig. 3.6. Fitting for Angle 60: Step 4.

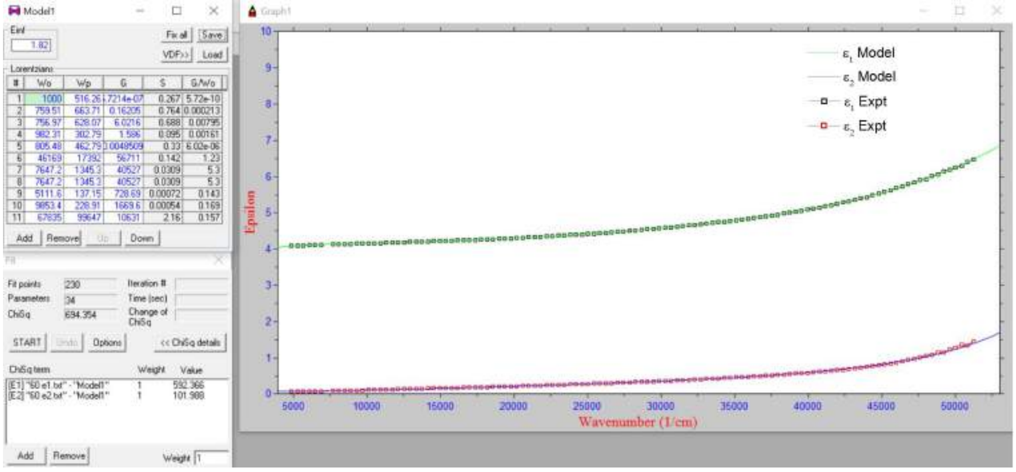

Einf 1.82

Lorentzians

#	Wo	Wp	G	S	G/Wo
1	1000	516.26	.7214e-07	0.267	5.72e-10
2	759.51	663.71	0.16205	0.764	0.000213
3	756.97	628.07	6.0216	0.688	0.00795
4	982.31	302.79	1.586	0.095	0.00161
5	805.48	462.79	.0048509	0.33	6.02e-06
6	46169	17392	56711	0.142	1.23
7	7647.2	1345.3	40527	0.0309	5.3
8	7647.2	1345.3	40527	0.0309	5.3
9	5111.6	137.15	728.69	0.00072	0.143
10	9853.4	228.91	1669.6	0.00054	0.169
11	67835	99647	10631	2.16	0.157

Fit points 230
Parameters 34
ChiSq 694.354
Iteration #
Time (sec)
Change of ChiSq

ChiSq term	Weight	Value
[E1] "60 e1.txt" - "Model1"	1	592.366
[E2] "60 e2.txt" - "Model1"	1	101.988

Weight 1

Fig. 3.7. Fitting for Angle 60: Step 5.

3.1.4 Fitting for 4 Angles: 50, 60, 70, 80

A similar approach is applied to the fitting for 4 angles. Fig. 3.8 illustrates the fitting for 4 angles at the fifth step. χ^2 did not decrease significantly, with a magnitude of 10^6. The major contributer comes from ϵ_1, especially at 80°. From the χ^2 contribution and Fig. 3.1, we conducted fitting for 50° and 60° followed by 70° and 80°. χ^2 for 50° and 60° reduced drastically to 9218, whereas that of 70° and 80° remains at 10^6. This might suggest a presence of anisotropy in the $LaAlO_3$ substrate.

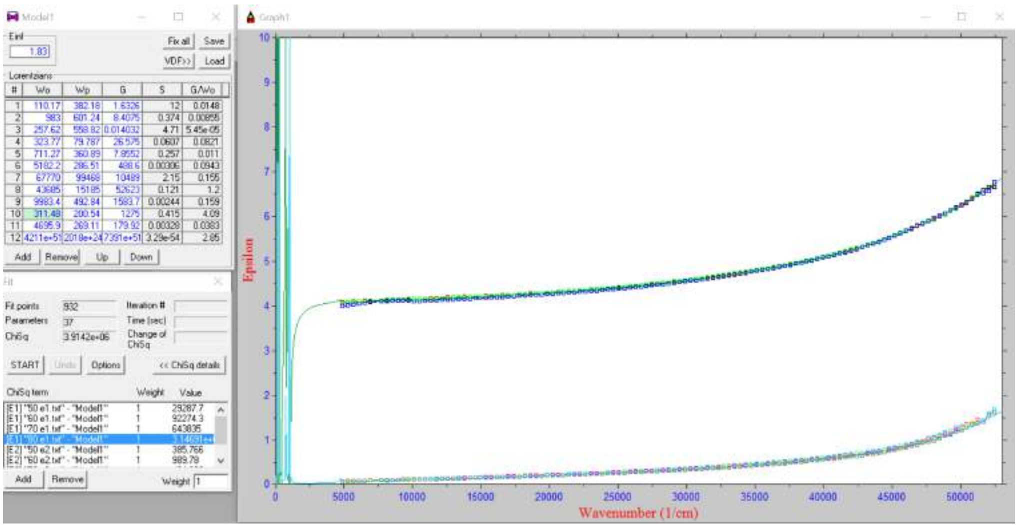

Einf: 1.83

Lorentzians

#	Wo	Wp	G	S	G/Wo
1	110.17	382.18	1.6326	12	0.0148
2	983	601.24	8.4075	0.374	0.00855
3	257.62	558.82	0.014032	4.71	5.45e-05
4	323.77	79.787	26.575	0.0607	0.0821
5	711.27	360.89	7.8552	0.257	0.011
6	5182.2	286.51	488.6	0.00306	0.0943
7	67770	99468	10489	2.15	0.155
8	43685	15185	52623	0.121	1.2
9	9983.4	492.84	1583.7	0.00244	0.159
10	311.48	200.54	1275	0.415	4.09
11	4695.9	269.11	179.92	0.00328	0.0383
12	4211e+51	2018e+24	7391e+51	3.29e-54	2.85

Fit points: 932
Parameters: 37
ChiSq: 3.9142e+06

ChiSq term	Weight	Value
[E1] "50 e1.txt" - "Model1"	1	29287.7
[E1] "60 e1.txt" - "Model1"	1	92274.3
[E1] "70 e1.txt" - "Model1"	1	643835
[E1] "80 e1.txt" - "Model1"	1	3.14691e+
[E2] "50 e2.txt" - "Model1"	1	385.766
[E2] "60 e2.txt" - "Model1"	1	989.78

Weight: 1

Fig. 3.8. Fitting for 4 Angles: Step 5.

3.1.5 Presence of Anisotropy

Fig. 3.9 illustrates the percentage difference for ϵ_1 and ϵ_2 with respect to 80°. The percentage difference is calculated as follow:

$$\frac{\mid \epsilon_1^i - \epsilon_1^{80} \mid}{\mid \epsilon_1^i + \epsilon_1^{80} \mid /2} \times 100\% \tag{3.7}$$

where ϵ_1^{80} is ϵ_1 at 80°, and i is 50, 60 and 70. The percentage difference for ϵ_2 is measured as well.

The percentage difference for ϵ_1 is up to 2.25 %. ϵ_1 for 50°, 60° and 70° with respect to 80° is precise to a large extent. For ϵ_2, the percentage difference is greater than 10 % from 0.6 to 0.9 eV. In general, the percentage difference is largest for 50°, followed by 60° and 70°. Anisotropy might be present, especially between 0.6 to 0.9 eV. This is suggested from Fig. 1.13 as well.

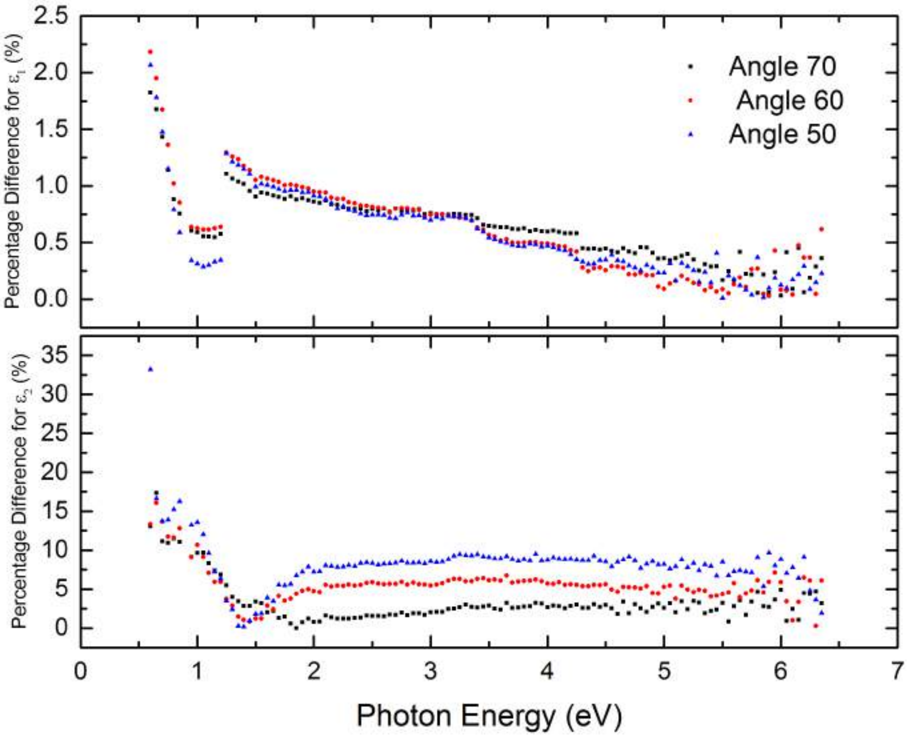

Fig. 3.9. Percentage Difference for ϵ_1 and ϵ_2 with respect to Angle 80.

3.1.6 Chi-Square Analysis

χ^2 acts as a metric for iterative fitting. The lowest χ^2 provides the most reliable results, although this is not always true. A good fit does not translate into a feasible model. Other forms of constraint could be implemented to justify the reliability of the results obtained. Our fitting procedure gave us the lowest χ^2 value of 694 for 60°. In general, a value of 1 for χ^2 represents a good fit. In this context, we can treat the $LaAlO_3$ as an anisotropic substrate to refine the analysis and further minimize χ^2.

3.2 Comparison with First-principles study by Xin Luo et al.

Fig. 3.10 illustrates the graph of ϵ_1 and ϵ_2 plotted as a function of photon energy. The literature "First-principles study of the electronic and optical properties in rhombohedral $LaAlO_3$" by X. Luo et al. obtained the experimental ϵ_1 and ϵ_2 and plotted them against the theoretical ϵ_1 and ϵ_2 computed with the FP-LAPW (Full-Potential linearized augmented plan wave) method in the framework of the density functional theory.

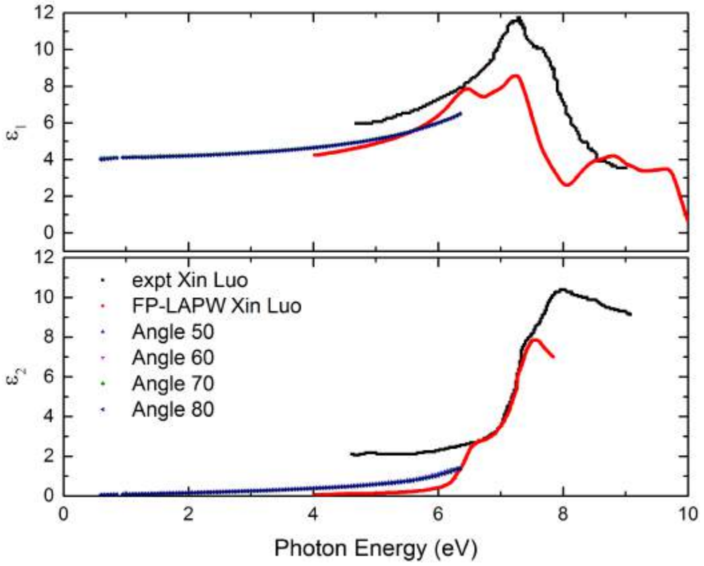

Fig. 3.10. ϵ_1 and ϵ_2 plotted as a function of photon energy (eV). Comparison of our experimental data points were made with the experimental and FP-LAPW parameters extracted from X. Luo et al. [5]

We compared our experimental ϵ_1 and ϵ_2 with the literature in the photon energy range of 4 to 6.35 eV. An increasing trend was observed for ϵ_1. The expt Xin Luo data points deviate from the FP-LAPW Xin Luo data points to a greater extent as compared to our experimental data.

For ϵ_2, the expt Xin Luo data fit closely with the FP-LAPW Xin Luo data from 6.5 to 7.5 eV. Below 6.5 eV, the value of ϵ_2 is approximately 2. The experimental bandgap of $LaAlO_3$ is 5.6 eV [12], therefore absorption ceases to exist below 5.6 eV. The extinction coefficient k will be very close to zero.

Since ϵ_2 = 2nk, we should observe a value that is approximately zero for ϵ_2 below 5.6 eV as depicted by our experimental data. ϵ_2 of expt Xin Luo below 5.6 eV is inaccurate.

3.3 Gold Nanoparticle Solution

3.3.1 Loss of Gold Nanoparticle Solution

The experiment was set up according to Section 2.3. The initial plan was to collect a set of measurement at 50°, 60° and 70°. During the measurement, we observe a decrease in the volume of gold nanoparticle solution. This led to a variation in the film thickness. To overcome this problem, the solution was left to dry up till a stain was formed. We proceed with the second set of measurement with the new setup. To ensure that the gold nanoparticles are present in the stain, we compare the pseudo dielectric function of Au NPs on $LaAlO_3$ substrate with that of the $LaAlO_3$ substrate before we proceed with any analysis. As illustrated in Fig. 3.11, we observed differences in the spectra. The difference signifies the presence of the gold nanoparticle on the $LaAlO_3$ substrate.

Next, we calculate the percentage difference of ψ and Δ between the two sets of measurement. Fig. 3.12 illustrates the percentage difference at 50°, 60° and 70°. From the percentage difference, it can be concluded that the solution and the stain produce different spectra. The second set of measurement is more reliable, as the film thickness does not vary during the experiment.

3.3.2 Ellipsometry Parameters

Fig. 3.13 illustrates ψ and Δ of AuNPs on $LaAlO_3$ substrate from 0.5 to 6.5 eV. We observe a greater variation in the ellipsometry parameters, compared to Fig. 3.1. This is due to the optical interference present in a

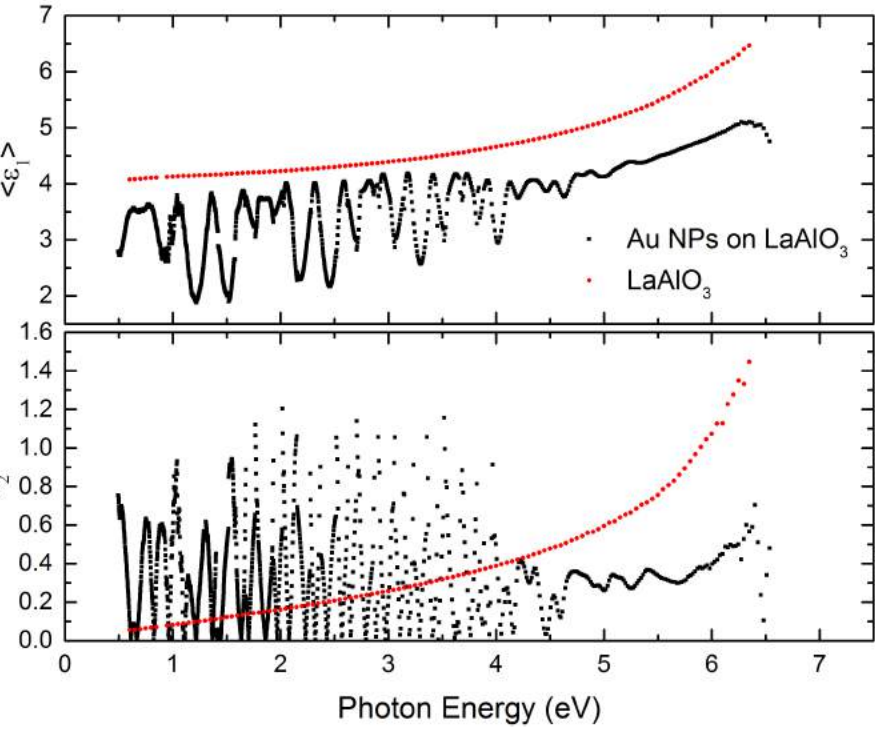

Fig. 3.11. Pseudo Dielectric Function of Au NPs on $LaAlO_3$ substrate with that of the $LaAlO_3$ substrate.

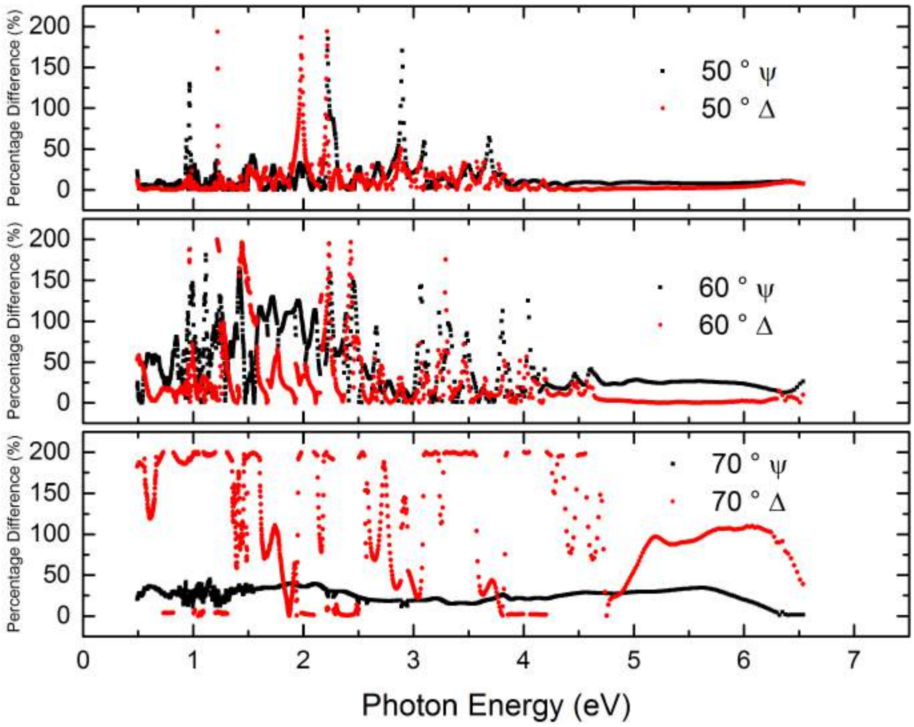

Fig. 3.12. Percentage Difference of the first experiment dataset ψ and Δ at 50°, 60° and 70° with respect to the second one.

thin film. This increases the difficulty in the fitting process.

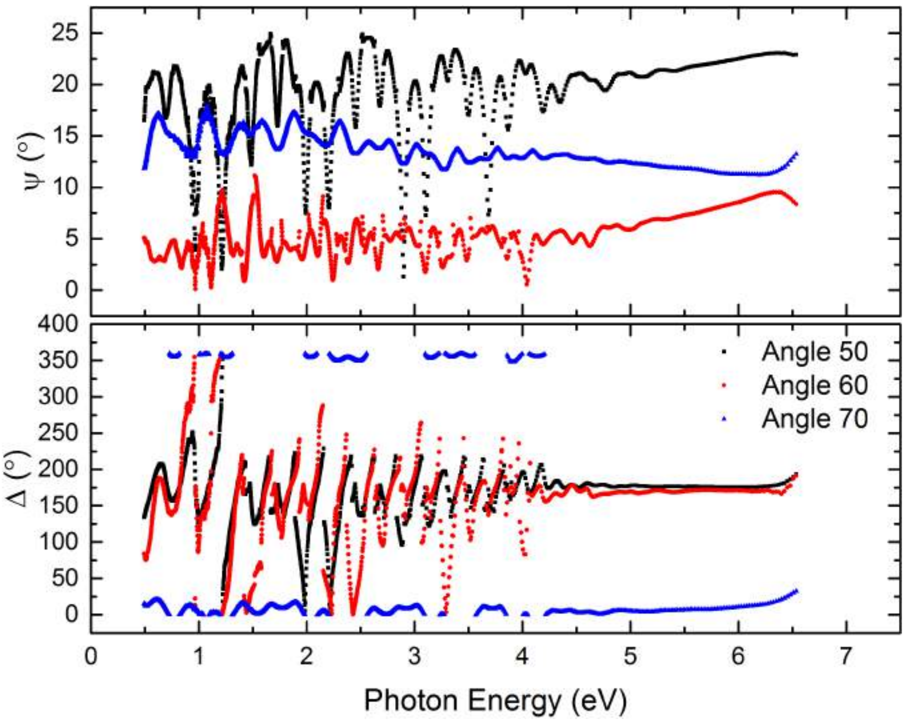

Fig. 3.13. ψ and Δ of AuNPs on $LaAlO_3$ substrate for 50°, 60° and 70° from 0.5 to 6.5 eV.

3.3.3 Fitting for Angle 60

Using a thin film on substrate optical model, we attempt to extract the relevant optical data of citrate coated gold nanoparticles on $LaAlO_3$ substrate. Fig. 3.14 illustrates the fitting procedure conducted in RefFIT. Using code -33, Model 1 represents the two layer optical model. The 1st row shows the angle of incidence: 60° as well as the polarizer angle: 45°. The second and third row denotes the gold nanoparticles and $LaAlO_3$ respectively. Their dielectric functions are represented by Model 2 and 3 respectively. Model 2 illustrates the dielectric function in Fig. 3.5. The parameters are fixed for the $LaAlO_3$ substrate. We are unable to fit the experimental parameters to the model.

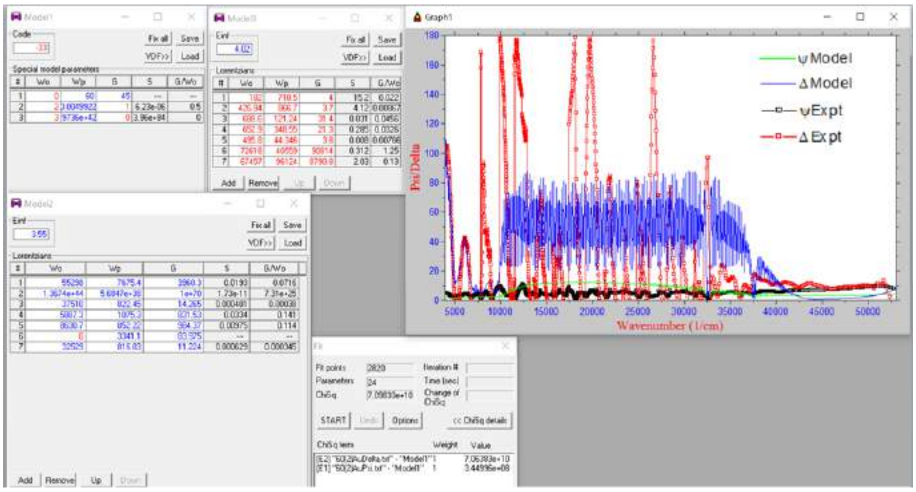

Code: -33

Special model parameters

#	Wo	Wp	G	S	G/Wo
1	0	90	45	---	---
2	2	.0049922	1	6.23e-06	0.5
3	3	9736e+42	0	3.96e+84	0

Model3

Einf: 4.02

Lorentzians

#	Wo	Wp	G	S	G/Wo
1	102	710.5	4	15.2	0.022
2	426.94	866.7	3.7	4.12	0.00867
3	688.6	121.24	31.4	0.031	0.0456
4	652.9	348.55	21.3	0.285	0.0326
5	495.8	44.346	3.8	0.008	0.00766
6	72618	40559	90814	0.312	1.25
7	67457	96124	8790.9	2.03	0.13

Model2

Einf: 3.55

Lorentzians

#	Wo	Wp	G	S	G/Wo
1	55290	7675.4	3960.3	0.0193	0.0716
2	1.3674e+44	5.6847e+38	1e+70	1.73e-11	7.31e+25
3	37510	822.45	14.265	0.000481	0.00038
4	5867.3	1075.3	831.53	0.0334	0.141
5	8630.7	852.22	984.37	0.00975	0.114
6	0	3341.1	83.975	---	---
7	32529	815.03	11.224	0.000629	0.000345

Fit

Fit points: 2820
Parameters: 24
ChiSq: 7.09833e+10
Iteration #:
Time (sec):
Change of ChiSq:

ChiSq items	Weight	Value
[E2] "60(2)AuDelta.txt" - "Model1"	1	7.06383e+10
[E1] "60(2)AuPsi.txt" - "Model1"	1	3.44996e+08

Fig. 3.14. Fitting for gold nanoparticles on $LaAlO_3$ substrate at 60°

Chapter 4

Conclusion

The dielectric function of $LaAlO_3$ was extracted from the ellipsometry parameters using the pseudo dielectric function. Fitting procedures were conducted in RefFIT as illustrated in Section 3.1.3. The lorentz oscillators obtained were used as part of the fitting procedure for the gold nanoparticles on $LaAlO_3$ substrate. The optical model must be improved to obtain a better fit. The large χ^2 and a significant percentage difference of ϵ_2 from 0.6 to 0.9 eV suggests the presence of anisotropy. The experimental ϵ_1 and ϵ_2 were compared with the literature by X. Luo et al.[5]. Based on the experimental band gap of $LaAlO_3$, the experiment ϵ_2 from X. Luo et al. below 5.6 eV is inaccurate.

4.1 Future Work

This project serves as a preliminary analysis, where we obtain the relevant direction for future work. The optical model for the gold nanoparticles on $LaAlO_3$ substrate could be improved with the Maxwell Garnett model. This will be a 4 layer optical model, where the surface layer and the interface of the gold nanoparticles solution are added. In addition, we have treated $LaAlO_3$ as an isotropic substrate. An anisotropic approach for the $LaAlO_3$ substrate could improve based on the above analysis.

Bibliography

[1] R. Lévy, N. T. Thanh, R. C. Doty, I. Hussain, R. J. Nichols, D. J. Schiffrin, M. Brust, and D. G. Fernig, "Rational and combinatorial design of peptide capping ligands for gold nanoparticles," *Journal of the American Chemical Society*, vol. 126, no. 32, pp. 10 076–10 084, 2004.

[2] S. O. Kasap, *Principles of electronic materials and devices.* McGraw-Hill, 2006.

[3] H. Fujiwara, *Spectroscopic ellipsometry: principles and applications.* John Wiley & Sons, 2007.

[4] D. M. Kienzle, "Surface structures of the metal-oxide materials strontium titanate and lanthanum aluminate," Ph.D. dissertation, NORTHWESTERN UNIVERSITY, 2013.

[5] X. Luo and B. Wang, "First-principles study of the electronic and optical properties in rhombohedral laalo3," *Journal of Applied Physics*, vol. 104, no. 5, 2008. [Online]. Available: http://scitation.aip.org/content/aip/journal/jap/104/5/10.1063/1.2973671

[6] X. Chen, W. W. Qoutah, P. Free, J. Hobley, D. G. Fernig, and D. Paramelle, "Features of thiolated ligands promoting resistance to ligand exchange in self-assembled monolayers on gold nanoparticles," *Australian Journal of Chemistry*, vol. 65, no. 3, pp. 266–274, 2012.

[7] E. Pensa, E. Corts, G. Corthey, P. Carro, C. Vericat, M. H. Fonticelli, G. Bentez, A. A. Rubert, and R. C. Salvarezza, "The chemistry of the sulfurgold interface: In search of a unified model," *Accounts of Chemical Research*, vol. 45, no. 8, pp. 1183–1192, 2012, pMID: 22444437. [Online]. Available: http://dx.doi.org/10.1021/ar200260p

[8] H. Häkkinen, "The gold-sulfur interface at the nanoscale," *Nature chemistry*, vol. 4, no. 6, pp. 443–455, 2012.

[9] V. G. Sathe and A. Dubey, "Broken symmetry in laalo 3 single crystal probed by resonant raman spectroscopy," *Journal of Physics: Condensed Matter*, vol. 19, no. 38, p. 382201, 2007. [Online]. Available: http://stacks.iop.org/0953-8984/19/i=38/a=382201

[10] T. Willett-Gies, E. DeLong, and S. Zollner, "Vibrational properties of bulk laalo3 from fourier-transform infrared ellipsometry," *Thin Solid Films*, vol. 571, Part 3, pp. 620 – 624, 2014, 6th International Conference on Spectroscopic Ellipsometry (ICSE-VI). [Online]. Available: http://www.sciencedirect.com/science/article/pii/S004060901302049X

[11] T. Asmara, A. Annadi, I. Santoso, P. Gogoi, A. Kotlov, H. Omer, M. Motapothula, M. Breese, M. Rübhausen, T. Venkatesan *et al.*, "Mechanisms of charge transfer and redistribution in laalo3/srtio3 revealed by high-energy optical conductivity," *Nature communications*, vol. 5, 2014.

[12] S.-G. Lim, S. Kriventsov, T. N. Jackson, J. H. Haeni, D. G. Schlom, A. M. Balbashov, R. Uecker, P. Reiche, J. L. Freeouf, and G. Lucovsky, "Dielectric functions and optical bandgaps of high-k dielectrics for metal-oxide-semiconductor field-effect transistors by far ultraviolet spectroscopic ellipsometry," *Journal of Applied Physics*, vol. 91, no. 7, 2002.